Connectomic and behavioral alterations in creatine transporter deficiency are partially normalized by gene therapy

Caterina Montani[1*], Alberto Galbusera[1], Bianca D'Epifanio[1], Elsa Ghirardini[2,3], Sara Cornuti[4], Jean-Charles Rene' Pasquin Mariani[1], A. Elizabeth De Guzman[1], Sine Mandrup Bertozzi[5], Andrea Armirotti[5], Laura Baroncelli[2,3+] and Alessandro Gozzi[1+]

[1]Functional Neuroimaging Laboratory, Istituto Italiano di Tecnologia, Center for Neuroscience and Cognitive Systems, CNCS@UNITN, Rovereto, Italy
[2]Department of Developmental Neuroscience, IRCCS Stella Maris Foundation, Pisa, Italy
[3]Institute of Neuroscience, National Research Council (CNR), Pisa, Italy
[4]BIO@SNS lab, Scuola Normale Superiore di Pisa, Pisa, Italy
[5]Analytical Chemistry Facility, Istituto Italiano di Tecnologia, Genova, Italy

[*] Current address: IRCCS Ospedale Policlinico San Martino, Genova, Italy
[+] Contributed equally

Correspondence: Alessandro Gozzi (alessandro.gozzi@iit.it); Caterina Montani (caterina.montani@hsanmartino.it)

Abstract

Creatine Transporter Deficiency (CTD) is an X-linked disease due to the loss of *SLC6A8* gene and presenting with low brain creatine, intellectual disability, autistic-like behavior and seizures. No treatments are available yet for CTD, and little is known about the brain circuit alterations underlying its pathological endophenotypes. Here, we tracked brain network and behavioral dysfunction in a murine model of CTD at two stages of disease progression. fMRI mapping revealed widespread disruption of brain connectivity in Slc6a8-KO mutants, with prominent somato-motor dysconnectivity in juvenile mice, and weaker and more focal cortical and subcortical hypoconnectivity in adults. Notably, perinatal AAV-mediated expression of human *SLC6A8* in Slc6a8-KO mutants significantly rescued juvenile fMRI hypoconnectivity. This effect was paralleled by a regression of translationally relevant phenotypes, including a reduction in stereotyped movements and increased body weight which persisted into adulthood. Cognitive deficits and residual fMRI hypoconnectivity in adult mice were instead not reverted by gene therapy. Finally, multivariate modeling in adult mice revealed a basal forebrain network whose activity was associated with behavioral performance, and modulated by brain creatine levels. This brain-behavior relationship was disrupted in Slc6a8-KO mutants. Our results document robust network disruption in CTD and demonstrate that CTD pathology can be partially reversed by perinatal genetic expression of *SLC6A8*, thus laying the basis for the development of experimental therapies for this genetic disorder.

Introduction

Creatine Transporter Deficiency (CTD, OMIM: #300352) is an X-linked disease originating from mutations of the solute carrier family 6-member 8 (*SLC6A8*) gene (Salomons et al., 2001). *SLC6A8* encodes the protein responsible for cellular creatine (Cr) uptake. The clinical manifestation of CTD follows lack of Cr in the brain and is predominantly neurological. It includes global developmental delay, mild to severe intellectual disability (ID), disturbance of expressive and cognitive speech, psycho-motor impairment, autistic-like behavior, and seizures (van de Kamp et al., 2014; Ghirardini et al., 2021). Despite our increased understanding of the etiopathological cascade underlying CTD (Joncquel-Chevalier Curt et al., 2015; Ghirardini et al., 2021), effective treatments for this monogenic disorder are lacking. Dietary supplementation with Cr, either alone or in combination with its synthesis precursors, has shown very limited success (van de Kamp et al., 2014; Ghirardini et al., 2021). Indeed, loss-of-function of *SLC6A8* not only prevents transport of Cr across the plasmatic membrane, but also affects its endogenous synthesis, which requires the coordinated action of multiple cell populations (Braissant et al., 2010; Baker et al., 2021). As a result, the current standard of care for CTD only involves pharmacological control of epilepsy and other CTD symptomatology.

Over the last few years, studies in murine models have revealed that neurological damage produced by CTD does not stem from overt neuronal death or degeneration, but it rather reflects more subtle alterations in synaptic compartments. Specifically, our own work previously documented a loss of GABAergic synapses in the cerebral cortex of mice lacking *Slc6a8* (Slc6a8-KO). This effect was associated with a dysfunction of parvalbumin-expressing GABAergic interneurons (Baroncelli et al., 2016; Ghirardini et al., 2023). Supporting a key etiopathological role of altered inhibitory transmission in CTD, we also described marked abnormalities in EEG neural oscillations, with decreased theta/alpha power and increased gamma activity in both Slc6a8-KO mice and CTD patients (Mazziotti et al., 2020). Owing to the key contribution of oscillatory activity in coordinating large-scale patterns of brain synchronization and interareal communication (Fries, 2015), this observation suggests that the neurological alterations that characterize CTD may be partly due to impaired long-range functional connectivity (Womelsdorf et al., 2007). This notion is consistent with neuroimaging observations in CTD patients, where abnormalities in anatomical connectivity (including white matter demyelination, and corpus callosum thinning) have been reported (van de Kamp et al., 2013).

Here, we used fMRI connectivity mapping (Liska et al., 2018; Pagani et al., 2019) and behavioral testing in Slc6a8-KO mice to (i) longitudinally track the neural circuits primarily affected in CTD and (ii) relate connectivity alterations to the behavioral deficits that characterize this disorder. Importantly, we also probed whether perinatal adeno-associated virus (AAV)-mediated expression of a functional *SLC6A8* transgene could restore proper creatine transporter (CRT) expression and Cr level in the brain, and thus rescue the observed connectomic and behavioral

phenotypes. Our results show that CTD is associated with distinct alterations in functional connectivity that evolve along its pathological trajectory. We also found that early intracerebral expression of human *SLC6A8* (hSLC6A8) may partly ameliorate both dysconnectivity and behavioral impairment in Slc6a8-KO mice. These results provide proof-of-concept evidence that CTD phenotypes may be partly reversed by genetic therapies aimed at reinstating homeostatic Cr levels.

Results

Creatine deficiency disrupts fMRI connectivity in cortical and subcortical brain regions

To probe whether CTD affects interareal functional connectivity, we carried out resting-state fMRI (rsfMRI) measurements (Gozzi and Schwarz, 2016; Gozzi and Zerbi, 2022) in Slc6a8-KO mice and control littermates (WT) at two different stages of disease progression. Specifically, we longitudinally mapped fMRI connectivity in the same mice at postnatal day 40 (P40) and in adulthood (P140), corresponding to early and late pathological stage, respectively.

To obtain a spatially-unbiased mapping of genotype-specific differences in fMRI connectivity we used Network Based Statistics (NBS) using a whole-brain network parcellation (Zalesky et al., 2010; Pagani et al., 2019). This analysis revealed the presence of diffuse hypo-connectivity in multiple brain regions of Slc6a8-KO mice both at P40 and P140 (Fig. 1). The spatial extent and magnitude of the observed changes, however, were largely different across the probed ages. In juvenile mice, fMRI hypo-connectivity was distributed across multiple cortical and subcortical regions, with a prominent involvement of somatosensory and motor cortices as well as hippocampal and thalamic areas (Fig. 1a,b). In contrast, fMRI hypoconnectivity in CTD mutants at P140 was weaker and more focal, encompassing the motor cortex and subcortical regions such as the striatum, the hypothalamus and some thalamic areas (Fig. 1c,d).

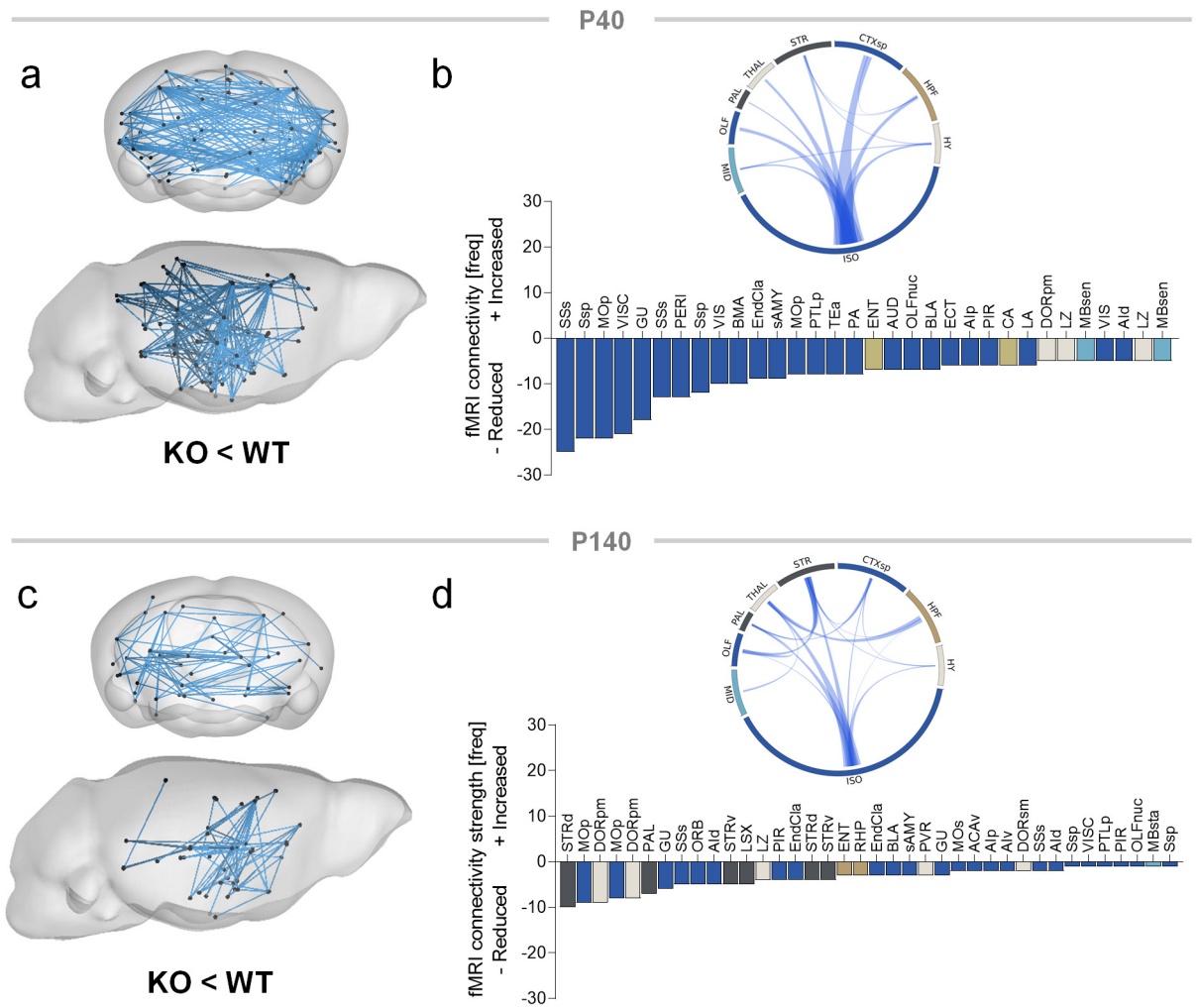

*Figure 1. **Reduced long-range fMRI connectivity in Slc6a8-KO mice.** fMRI connectivity alterations in Slc6a8-KO mice as assessed with NBS at P40 (a, b) and P140 (c, d; t> |2.7| for both comparisons). Histograms represent the number of links exhibiting reduced connectivity in Slc6a8-KO mice at P40 and P140, respectively. Circular plots in (b) and (d) illustrate corresponding patterns of altered interareal connectivity. In these plots, individual brain areas have been grouped into 9 anatomical meta regions. Thickness of links in circular plots is proportional to the relative number of affected links. The complete list of brain areas (and abbreviations) used for NBS is reported in Table S1.*

To further investigate the circuit-level substrates differentially affected by CTD, we next used a seed-based analysis to probe fMRI connectivity in some of the brain regions exhibiting large effect-size in NBS (Fig. 1). This investigation revealed robustly reduced inter-hemispheric connectivity in somatomotor areas of Slc6a8-KO mice at P40 (Fig. 2a-d), and to a lower extent also at P140 (Fig. 2e,h; Supplementary Fig. 1). At P40, mutant mice also showed reduced thalamo-hippocampal and frontocortical connectivity, but no alterations in striatal regions (Supplementary Fig. 1). In contrast, the striatum represented one of the primary hubs of hypoconnectivity in Slc6a8-KO mice at P140, with evidence of functional disconnection of this region with thalamic nuclei (Fig. 2f,h). Adult Slc6a8-KO mice also exhibited foci of reduced fMRI connectivity in thalamo-hippocampal

regions (Supplementary Fig. 1). Leveraging the longitudinal design of our investigation, we also examined the temporal evolution of connectivity in somato-motor and striatal circuits across the two timepoints tested (Supplementary Fig. 2). A pairwise quantification of connectivity in these networks did not reveal any difference in temporal trajectories across groups (Supplementary Fig. 2). Altogether, these findings reveal widespread disruption of brain connectivity in Slc6a8-KO mice, with robust somato-motor dysconnectivity in juvenile mice evolving into more focal cortical and subcortical hypoconnectivity in adulthood.

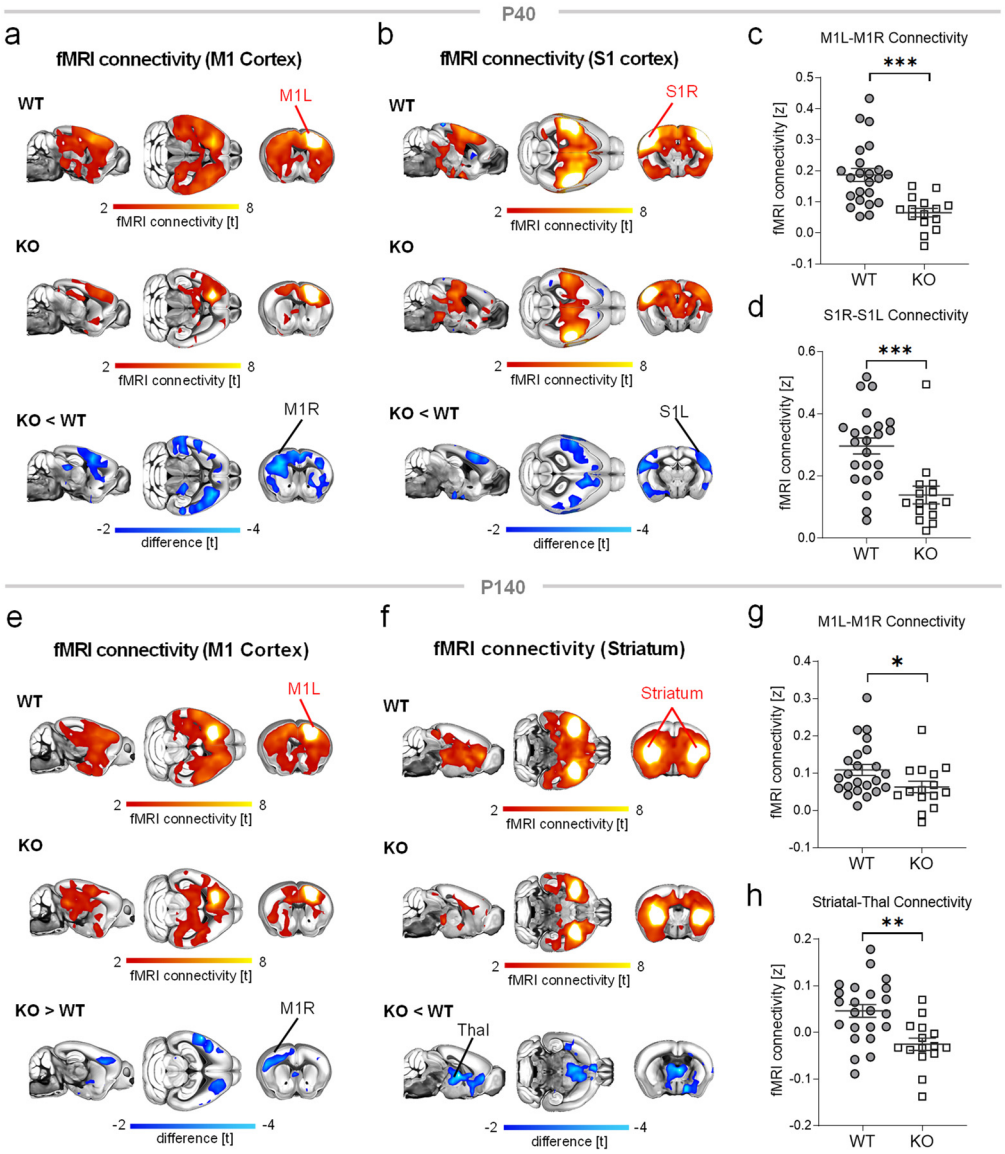

Figure 2. Networks exhibiting altered fMRI connectivity in Slc6a8-KO mice. *(a-d) Seed-correlation mapping highlighted disrupted somato-motor connectivity in Slc6a8-KO mice at P40. (e-h) fMRI connectivity in motor regions was disrupted also at P140. At this age we also found a prominent reduction of fMRI connectivity between striatal regions and the thalamus. Red/yellow indicates areas in the brain maps exhibiting significant (t> 2.1) fMRI connectivity with seed regions (indicated with red lettering). Blue indicates between-group connectivity differences (t-test, t> 2.1).*

*Corresponding quantifications of connectivity changes in the two groups are reported in panels c,d for P40 (S1 t = 4.02, p = 0.0003; M1 t = 4.3, p = 0.0001) and g,h for P140 (M1, t = 2.06, p = 0.046; Striatal-Thal, t = 3.55, p =0.001). L, left; R, right; M1, motor cortex; S1, somatosensory cortex; Thal, thalamus. All statistics are FWE cluster-corrected. FWE, family-wise error. *p < 0.05, **p < 0.01, ***p < 0.001. Error bars indicate SEM and dots represent individual values.*

AAV-mediated expression of human SLC6A8 rescues fMRI dysconnectivity in juvenile Slc6a8-KO mice

To probe the efficacy of genetic expression of exogenous CRT as putative therapy for CTD, we conducted intracerebroventricular (i.c.v.) injections of a novel AAV9-vector encoding a functional copy of the non-codon optimized human *SLC6A8* gene under the control of JeT promoter (AAV9/JeT-hSLC6A8, herein referred to as AAV-hSLC6A8). The AAV-hSLC6A8 vector was designed to leverage the wide biodistribution of AAV following i.c.v. perinatal injection (Fig. 3a,b) (Chen et al., 2023) and to allow broad and ubiquitous transgene expression via the use of JeT promoter (Chen et al., 2022). Our experimental goal was to induce early hSLC6A8 expression in forebrain regions such to minimize or prevent the emergence of pathological CTD-related phenotypes. By doing so, we sought to test whether perinatal AAV-mediated expression of hSLC6A8 represents a viable gene therapy for CTD. The AAV-hSLC6A8 vector was injected perinatally in newborn (P1) Slc6a8-KO mice and WT littermates (Fig. 3a). An analogous vector expressing GFP protein (AAV-GFP) was used as control condition in both genotypes. To assess the efficacy of this strategy, we carried out longitudinal fMRI and behavioral investigation.

Notably, NBS analysis of fMRI measurements revealed that AAV-hSLC6A8 administration robustly rescued fMRI hypo-connectivity in Slc6a8-KO mice at P40 (Fig. 3c,d). This effect entailed a marked increase of fMRI connectivity in virtually all the neocortical and subcortical regions that we found to be hypo-connected in Slc6a8-KO mice injected with AAV-GFP. Seed-based mapping corroborated this result, showing that gene therapy could effectively restore somato-motor (Fig. 3e-h), and cingulate hypoconnectivity in Slc6a8-KO mice at P40 (Supplementary Fig. 3). In contrast, no appreciable connectivity normalization was observed in adulthood in the same mice, using NBS analysis ($p > 0.9$, $t < 0.1$, all links). Accordingly, seed-based mapping did not reveal any anatomically-relevant fMRI connectivity rescue in AAV-hSLC6A8 treated mutant mice at P140 (Fig. 3i-l; Supplementary Fig. 3). Taken together, these results show that neonatal expression of hSLC6A8 robustly rescued juvenile fMRI dysconnectivity in Slc6a8-KO mice, but not the corresponding alterations in fMRI connectivity observed at a later pathological stages (i.e. P140).

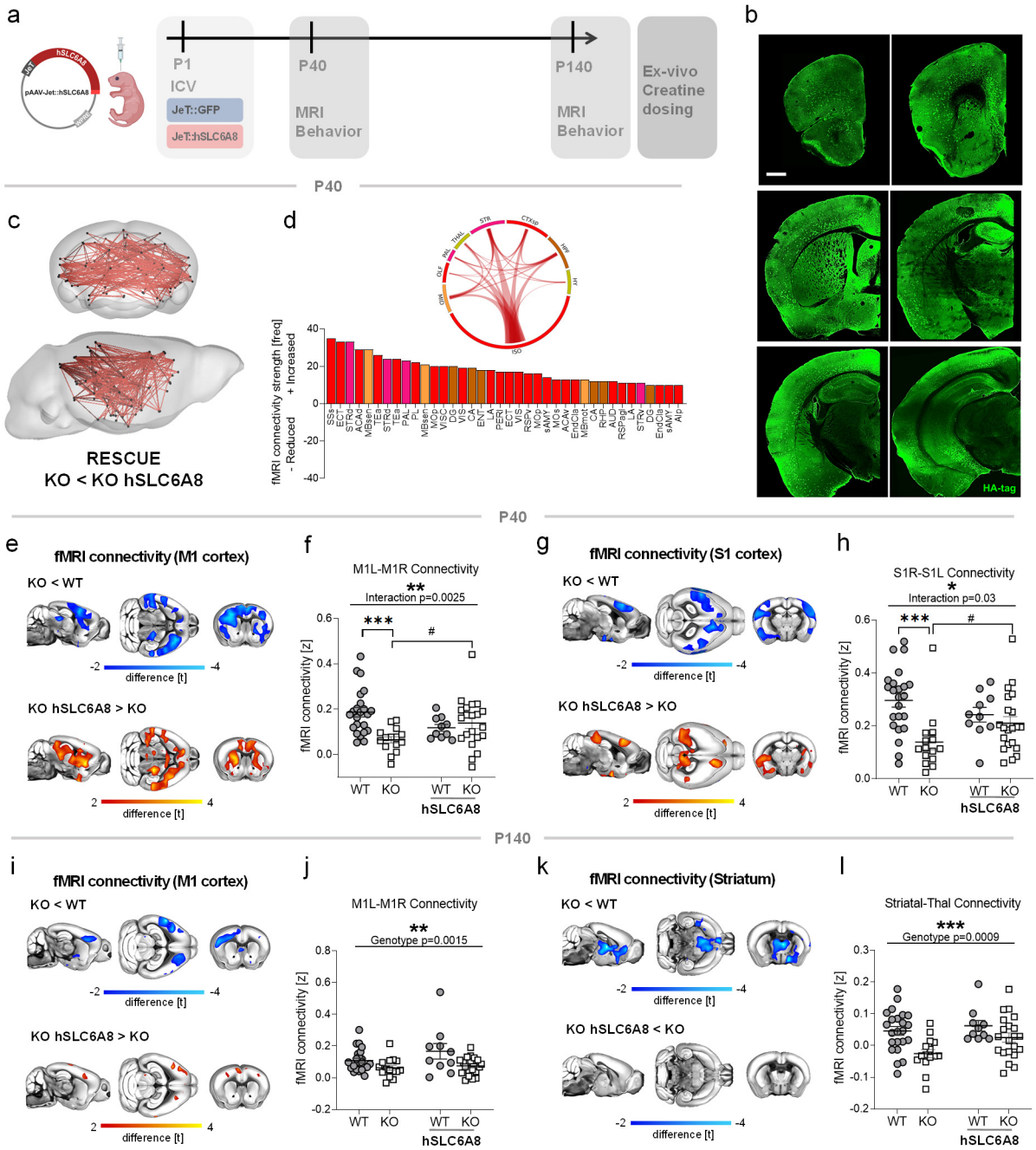

Figure 3. Perinatal AAV-hSLC6A8 injection rescues functional hypoconnectivity in juvenile Slc6a8-KO mice. *(a) Experimental design. (b) HA tag staining of exogenous CRT protein in mutant mice receiving AAV-hSLC6A8 injections at P1. Coronal sections (20X magnification). Scale bar: 1.5 mm. (c) NBS highlighted increased fMRI connectivity at P40 in Slc6a8-KO mice injected with AAV-hSLC68 vector compared to GFP-treated mutants (red, t > |3|). (d) Connectivity links exhibiting a significant rescue in Slc6a8-KO mice after AAV-hSLC6A8 injection at P1 and regional quantification in circular plots. (e-h) Seed-correlation mapping revealed rescue of interhemispheric connectivity in the somato-motor cortex of juvenile Slc6a8-KO mice treated with AAV-hSLC6A8. Red/yellow coloring in bottom panels denotes the rescue effects of AAV- hSLC6A8 treatment (t-test, t> 2). Plots report quantification of connectivity strength between seed and regions exhibiting rescue of connectivity (f, M1: Two-way ANOVA, genotype x treatment interaction F =9.86, p =0.0025; t-test, # p < 0.05; ### p < 0.001; h, S1: Two-way ANOVA, interaction F = 4.76, p = 0.033; Mann Whitney test # p < 0.05, t-test, ### p < 0.001). The same analysis at P140 revealed no effect of gene therapy in either motor cortex (j; Two-way*

*ANOVA, genotype factor F = 11.04, p = 0.0015, interaction F =1.24, p = 0.27) or the striatum-thalamus network (l; Two-way ANOVA, genotype factor F = 12.03, p = 0.0009, interaction F = 1.20, p = 0.28). L, left; R, right; S1, somatosensory cortex; M1, motor cortex; Thal, thalamus. All statistics are FWE cluster-corrected. FWE, family-wise error. For Two-way ANOVA, * p< 0.05, **p< 0.01, ***p < 0.001. Error bars indicate SEM and dots represent individual values. The complete list of brain areas (and abbreviations) used for NBS is reported in Table S1.*

AAV-mediated expression of human SLC6A8 improves autistic-like behavior in SLC6A8-KO mice

We previously reported that Slc6a8-KO mice exhibit a number of traits and phenotypes of translational relevance for CTD, including reduced body weight, cognitive impairment and autistic-like behavior (van de Kamp et al., 2013; Baroncelli et al., 2016). To assess whether perinatal gene therapy could prevent the onset of CTD-relevant pathological manifestations, we probed working memory (using the Y maze task) and stereotyped movements (via self-grooming scoring), and recorded body weight at P40 and P140 in mice injected with either AAV-hSLC6A8 or AAV-GFP (Fig. 4).

Slc6a8-KO mice at P40 did not show increased grooming behavior (Fig. 4a), but exhibited significantly decreased spontaneous alternation in the Y maze (Fig. 4b), and reduced body weight compared to WT mice (Fig. 4c). The same mice showed significantly increased grooming (Fig. 4e), decreased spontaneous alternations (Fig. 4f) and robustly reduced body weight at P140 (Fig. 4g), thus recapitulating our previous findings (Baroncelli et al., 2016).

Perinatal gene therapy produced a significant amelioration of some of these pathological traits. Specifically, at P40 we found a moderate (≈15%) recovery of body weight of Slc6a8-KO mice, but no effect on behavioral performance in the spontaneous alternation test. Remarkably, at P140 AAV-hSLC6A8 treatment completely prevented the appearance of increased grooming in Slc6a8-KO mutants. This effect was accompanied by a partial (≈20%) recovery of body weight. However, as seen in juvenile mice, gene therapy failed to improve behavioral performance in the spontaneous alternation task at this disease stage. The inclusion of a group of WT mice receiving an AAV-hSLC6A8 injection allowed us also to investigate the behavioral effect of CRT overexpression. We noted a slight deterioration of behavioral performance in the Y maze task in WT mice receiving the AAV-hSLC6A8 vector (Fig. 4b,f), as well as increased baseline exploratory activity (i.e., number of arm entries) in both Slc6a8-KO and WT mice injected with AAV-hSLC6A8 (Supplementary Fig. 4). Altogether, these data demonstrate that perinatal gene therapy in Scl68a-KO mice can mitigate some pathological traits of high translational relevance for CTD, including autism-like motor stereotypies.

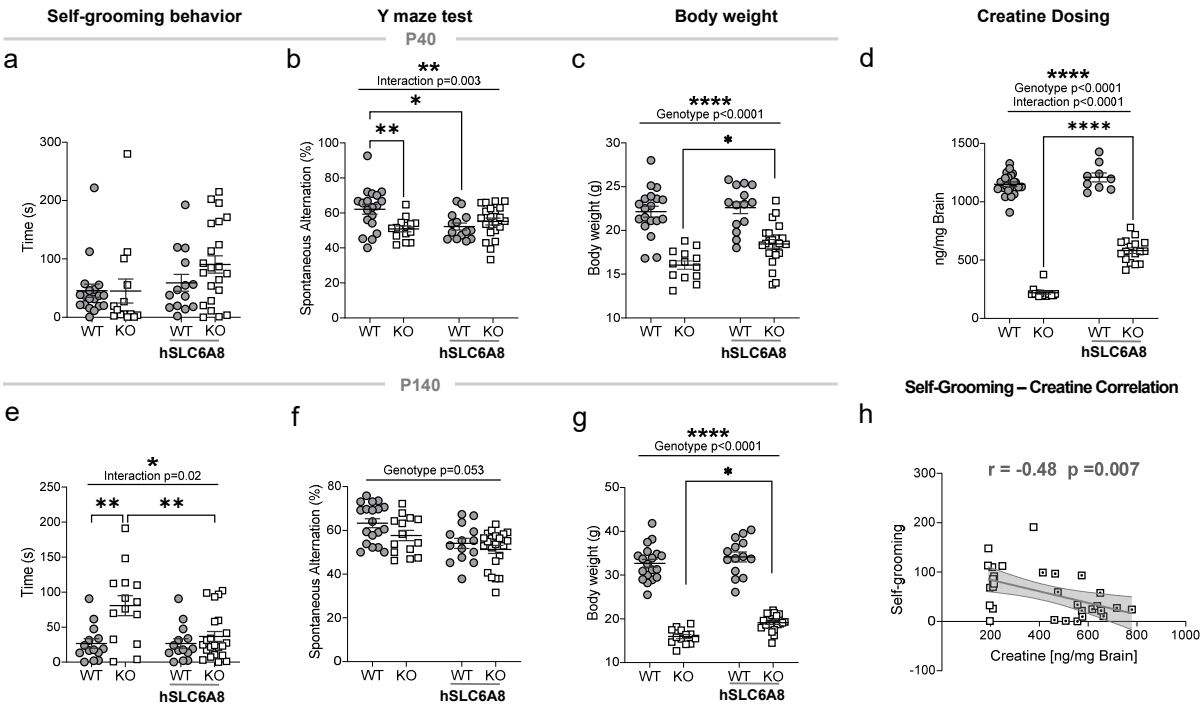

Figure 4. Perinatal AAV-hSLC6A8 injection increases body weight and prevents the onset of autistic-like stereotypies in adult Slc6a8-KO mice. *(a-c) Time spent self-grooming (a, Two-way ANOVA, genotype x treatment interaction F = 1.06, p = 0.31), spontaneous alternation in the Y maze task (b, Two-way ANOVA, interaction F = 9.26, p = 0.003) and body weight (c, Two-way ANOVA, genotype factor F = 74.4, p < 0.0001, interaction F = 2.74, p = 0.10,) in the four experimental groups at P40. d) Quantification of brain creatine levels at P140 (Two-way ANOVA, genotype factor F = 1094, p < 0.0001, interaction F = 41.33, p < 0.0001). e) The increased grooming behavior of Slc6a8-KO mice at P140 is completely rescued by AAV- hSLC6A8 injection (Two-way ANOVA, interaction F = 5.76, p = 0.02), while no effect was found in the Y maze (f, Two-way ANOVA, genotype factor F = 3.9, p = 0.053, interaction F = 0.47, p = 0.5). g) The weight of Slc6a8-KO mice injected with AAV-hSLC6A8 was significantly increased compared to Slc6a8-KO mice receiving the control vector (Two-way ANOVA, genotype factor F = 426.1, p < 0.0001, interaction F = 1.21, p = 0.27). h) Brain creatine levels negatively correlate with self-grooming scoring in Slc6a8-KO mice (Pearson r = -0.48, R squared = 0.23, p = 0.007). Error bars indicate SEM and each dot represents a mouse. Tukey's multiple comparison test, *p < 0.05, **p < 0.01, ***p < 0.001, ****p < 0.0001.*

Gene therapy with AAV-SLC6A8 increases brain creatine levels

Brain Cr depletion lies at the basis of the pathological cascade that determines CTD (van de Kamp et al., 2014; Ghirardini et al., 2021). It thus follows that the observed therapeutic effects of AAV-hSLC6A8 treatment on fMRI connectivity, motor stereotypies and body weight should reflect higher brain Cr levels. To verify that brain Cr content was effectively increased in experimental mice receiving AAV-hSLC6A8 injection, we measured post-mortem Cr levels in the brain of a randomly selected sub-cohort of experimental mice at the end of the last behavioral investigations at P140. These measurements showed that Cr levels in the brain of mice treated with AAV-hSLC6A8 were robustly increased (mean increase, ≈ 2.7-fold). This result indicates that AAV-mediated expression hSLC6A8 encodes significant amounts of functionally-active CRT protein

(Fig. 4d). It should be noted that the employed gene therapy was not able to fully reinstate physiological levels of Cr in Slc6a8-KO mice, as the average Cr content measured in mutant mice receiving AAV-hSLC6A8 was approximately half the amount measured in WT mice. In spite of this, we found an inverse relationship between Cr brain levels and self-grooming scoring in Slc6a8-KO mice treated with AAV-GFP or AAV-hSLC6A8 (Fig. 4h; Pearson $r = -0.48$; $p = 0.007$). A similar inverse relationship and slope was also noticeable in Slc6a8-KO mice receiving AAV-hSLC6A8 injections, although the effect in this cohort did not reach statistical significance (Fig. 4h; Pearson $r = -0.38$; $p = 0.16$). These results suggest that perinatal AAV-hSLC6A8 administration can effectively increase central levels of Cr, resulting in domain-specific amelioration of CTD pathology.

Connectivity of a mesolimbic-prefrontal circuit predicts behavioral performance, and is modulated by creatine levels

To obtain an unbiased mapping of the putative circuits underlying behavioral disruption in our CTD mouse, we used a multivariate model to associate cross-subject variance in fMRI connectivity with corresponding behavioral profiles. This was done using a partial least square correlation (PLS) analysis (McIntosh et al., 1996; Krishnan et al., 2011; Kebets et al., 2019, 2021) on fMRI connectivity data extracted from the cingulate cortex. The use of multivariate approaches like PLS reduces the bias related to the use of univariate brain/behavior correlations in relatively small samples, an approach that has been recently shown to be highly prone to false positives (Marek et al., 2022). Another advantage of PLS is the possibility to model, within the same framework, Cr levels as a continuous variable. Thus, using PLS we sought to identify areas whose connectivity covaries with (and thus putatively explains) the behavioral profile across multiple tests.

For each animal we modeled behavioral scores out of spontaneous alternation and grooming tests, and Cr levels measured at P140 (Fig 5). By including Cr levels as a continuous variable, we were able to assess whether the identified circuits are sensitive to Cr modulation. We probed connectivity of the cingulate cortex because this region projects to multiple brain areas that are relevant to the tests examined, including ventral hippocampus for spontaneous alternation, and striatal and mesolimbic areas for self-grooming (Kalueff et al., 2015; Pagani et al., 2021).

PLS analysis revealed one highly significant latent component (LC1; $p = 0.004$) accounting for 39.5% of the covariance between brain connectivity, behavioral performance and Cr levels. Regional mapping of the identified component revealed a prefrontal-basal-forebrain (i.e., insula, nucleus accumbens) circuit whose connectivity positively covaried with stereotyped behavior, but not spontaneous alternation, in WT mice (Fig 5a,b). This result is consistent with the known organization of the distributed network of regions that control stereotyped activity in rodents (Kalueff et al., 2015) and suggest that connectivity measurements we employed are behaviorally

relevant. Interestingly, this brain-behavior relationship was disrupted in Slc6a8-KO mice, where we found reversed covariance between behavioral scores and connectivity in the same network.

Importantly, Cr levels were also found to covary (and thus potentially modulate) the activity of this circuit, albeit with different directional effects in WT and Slc6a8-KO mice (Fig 5b,c). In control mice, Cr levels were inversely related to the activity in these regions, suggesting that non-homeostatic levels of Cr can negatively affect this circuit to impact behavior. In contrast, Cr levels were found to be positively related to behavioral performance in Slc6a8-KO mutants, a finding consistent with the ameliorating effect of AAV-mediated hSLC6A8 expression.

These results uncover a behaviorally-relevant prefrontal-basal-forebrain network whose activity is differentially modulated by Cr levels. This brain-behavior relationship was disrupted in Slc6a8-KO mutants, hence implicating aberrant prefrontal-mesolimbic connectivity in the pathology of CTD.

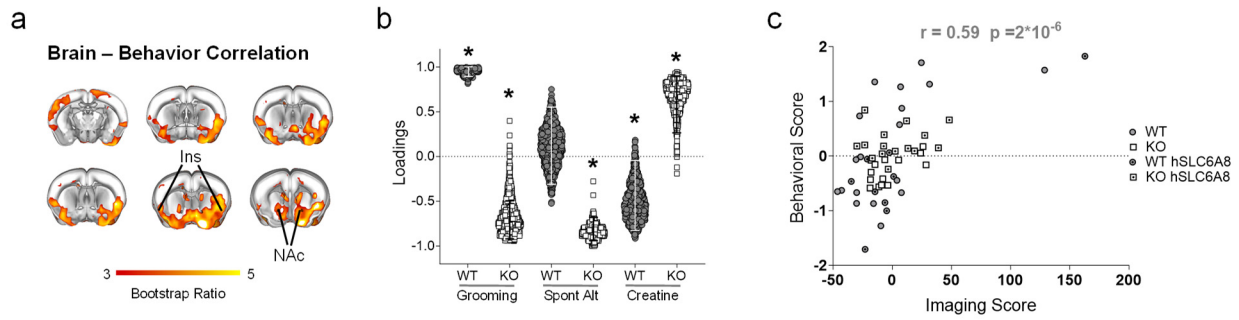

Figure 5. Multivariate modeling reveals disrupted brain-behavior relationship in Slc6a8-KO mice. *PLS analysis revealed a significant latent component (LC1) that explained around 40% of covariance between self-grooming, cingulate-striatal-insular network and Cr levels across mice. a) Red/yellow coloring represents bootstrap-ratio (BSR) z-scores obtained from 1000 bootstrapping iterations. The highlighted basal-forebrain and mesolimbic regions are those whose connectivity with the anterior cingulate exhibit robust covariance with behavioral performance and Cr levels as per the employed PLS model. b) Creatine and behavior loadings for LC1. Columns indicate the contribution of each observed variable to the LC and the directionality of covariance. Errors bars indicate 5th to 95th bootstrapping percentiles. Asterisk indicates a significant contribution to the overall PLS relationship for LC1 (relationship is non-zero, i.e., 95% CIs do not encompass 0 loading). c) PLS correlation between individual brain, Cr and behavior scores for LC1. Each dot indicates an individual mouse. Ins, Insular Cortex; NAc, Nucleus Accumbens.*

Discussion

Recent advancements in understanding the clinical manifestations and etiopathological course of CTD (van de Kamp et al., 2013, 2014; Ghirardini et al., 2021) have not been paralleled by a deeper comprehension of the systems-level dysfunction and mechanisms underlying this genetic syndrome. To fill this knowledge gap, we have employed longitudinal functional imaging, behavioral phenotyping and genetic therapy in an established murine model of CTD to investigate how Cr depletion affects brain connectivity and leads to the circuit dysfunctions that characterize CTD.

Our fMRI studies revealed robust functional hypoconnectivity both in juvenile and adult Slc6a8-KO mice, suggesting that Cr depletion leads to impaired large-scale interareal communication. We found fMRI hypoconnectivity to mostly affect cortical regions during early pathological stages, subsequently evolving into more prominent subcortical hypoconnectivity (especially in striatal, mesolimbic and thalamic areas) in adulthood. Although fMRI hypoconnectivity may reflect multifactorial mechanisms (Gozzi and Zerbi, 2022), our results are consistent with prior evidence of disrupted function and maintenance of synaptic circuits in Slc6a8-KO mice (Ghirardini et al., 2023). Synaptic coupling is a key determinant of long-range synchronization underlying fMRI connectivity, and recent investigations have revealed fMRI hyperconnectivity in autism-relevant mouse models exhibiting aberrant synaptic signaling (Pagani et al., 2021), as well as fMRI hypoconnectivity in mouse models showing reduced synaptic density (Liska et al., 2018; Pagani et al., 2019). In this respect, our results corroborate the notion that brain connectopathy is a hallmark endophenotype of multiple neurodevelopmental disorders associated with synaptic pathology (Pagani et al., 2021; Zerbi et al., 2021).

The observation of reduced fMRI connectivity in Slc6a8-KO mice is also in agreement with our previous study showing that Slc6a8-KO mice exhibit a severe epileptic phenotype and significant changes in neural oscillations, with lower power of theta/alpha EEG frequencies and increased power of beta/gamma bands (Mazziotti et al., 2020). Chemogenetic and pharmacological manipulations have indeed shown that fMRI hypoconnectivity can reflect reduced low frequency EEG power and concomitant broad-band increased in higher-frequency activity as a result of increased excitability and asynchronous firing (Montani et al., 2020; Rocchi et al., 2022). Thus, the effect of Cr deficiency on EEG power aligns with the observed reduction in fMRI connectivity (i.e., a measure of infraslow synchronization), potentially indicating a shift from slow, synchronized neural coherency to high frequency (yet asynchronous) activity. Similar spectral changes are present in the EEG of CTD children with respect to age-matched controls (Mazziotti et al., 2020), underscoring the translational value of the present study.

From a cellular standpoint, these alterations may be linked to prior studies pointing at a significant heterogeneity of *Slc6a8* expression across cell populations (Braissant et al., 2010; Saunders et al., 2018; Yao et al., 2021), and the observation that synaptic alterations in CTD mostly affect GABAergic interneurons (Baroncelli et al., 2016; Ghirardini et al., 2023). These alterations

may in turn lead to a generalized reduction of cortical inhibitory tone and a disruption of neural circuitry efficiency, two key pathological determinants associated with multiple neurodevelopmental disorders (Baroncelli et al., 2011). Given the crucial role of parvalbuminergic (PV) fast-spiking interneurons in the regulation of long-range functional synchronization (Sohal et al., 2009), the presence of morpho-physiological dysfunction of PV synapses in Slc6a8-KO mice (Ghirardini et al., 2023) might represent a plausible cellular correlate of the observed fMRI desynchronization. Accordingly, previous studies have shown that alterations of the excitatory/inhibitory ratio may perturb brain oscillatory activity and fMRI connectivity with potential specific contributions of different cell populations (Pagani et al., 2019; Rocchi et al., 2022).

The putative translational relevance of these imaging findings is further corroborated by the observation of decreased inter-hemispheric connectivity in Slc6a8-KO mice at both P40 and P140. Given the robust anatomical foundations of functional connectivity (Coletta et al., 2020) and the causal role of the corpus callosum in driving the synchronization of the two brain hemispheres (Owen et al., 2013; Roland et al., 2017; Siffredi et al., 2021), these findings may be functionally linked to previous anatomical MRI studies revealing corpus callosum thinning in CTD patients (van de Kamp et al., 2013).

Our study also serves as a preclinical investigation of the therapeutic potential of early gene therapy in preventing the pathological and behavioral manifestations of CTD. The chronic progressive morbidity of CTD represents a significant unmet clinical need for which gene therapy could potentially offer a lifelong treatment option. In this respect, CTD is an ideal target for gene additive therapy for three reasons: i) it is a monogenic condition; ii) the replenishment of brain Cr is effective in ameliorating the clinical manifestations of two other disorders caused by alterations in Cr metabolism (Stöckler et al., 1996; Battini et al., 2017); iii) heterozygous females for *Slc6a8* mutations show moderate Cr reduction and partial cognitive deficits (Van De Kamp et al., 2011; Hautman et al., 2014), suggesting that CTD phenotype exhibits a dose-dependent relationship with the expression of a functional gene.

In the present study, a single intraventricular infusion of AAV-hSLC6A8 in newborn Slc6a8-KO mice was sufficient to induce a widespread distribution of the transgene in the brain, resulting in a long-lasting increase in cerebral Cr levels. Importantly, while the resulting Cr concentration was approximately 50% less than the physiological Cr concentration measured in WT mice, postnatal reinstatement of CRT function led to partial or full rescue of some CTD-relevant endophenotypes, including functional brain hypoconnectivity in juvenile mice, reduced body weight, and the manifestation of autistic-like stereotyped behavior in adulthood. Interestingly, our PLS analysis linked these endophenotypes to the activity of a fronto-mesolimbic circuit whose function was disrupted in Slc6a8-KO mice, thus revealing a neural circuitry that could be key to the pathological manifestation of CTD, and whose function was modulated by Cr levels in adulthood.

These findings are consistent with previous studies showing that reinstatement of cerebral Cr metabolism via oral Cr supplementation can ameliorate the clinical symptoms in other neurodevelopmental syndromes associated with mutations of Cr synthetic enzymes (Schulze and Battini, 2007; Cacciante et al., 2020; Khoja et al., 2022).

Rather unexpectedly, AAV-mediated delivery of hSLC6A8 failed to improve cognitive performance in mutant mice. Several factors may contribute to this observation. Because optimal AAV expression requires about 2 weeks, our perinatal injection strategy might have failed to provide physiologically-relevant Cr levels during an early time-window of considerable importance for maturation of higher order cognitive functions (Udobi et al., 2019). In addition, the titre of the injected virus might not have reached the transduction threshold sufficient to induce a full recovery of the pathological endophenotype. Accordingly, the increase of Cr achieved with our treatment did not reproduce the physiological Cr level measured in the brain of WT mice, suggesting that full restoration of physiological Cr levels may be critical to the establishment of functional cognitive activity in CTD. In keeping with this, we recently reported a strictly dose-dependent therapeutic effect of cyclocreatine (a lipophilic Cr analogue that vicariate its metabolic function) on cognitive defects and stereotyped behavior in Slc6a8-KO mice, possibly reflecting distinct metabolic constraints of the different underlying brain processes (Cacciante et al., 2020). Moreover, a trend towards a deterioration of mnemonic performance was observed in AAV-treated WT mice, pointing at possible detrimental effects induced by overexpression of CRT above homeostatic levels in some cell clusters. Further preclinical studies are warranted to optimize CRT expression such to achieve physiological replenishment of Cr levels in the central nervous system of Slc6a8-KO mice.

In conclusion, our results document translationally relevant, systems-level disruption of brain activity in a murine model of CTD and provide key proof-of-concept evidence that early gene therapy holds potential as a disease modifying strategy or CTD. We expect these findings to help the development of experimental therapies for this currently untreatable genetic disorder.

Materials and Methods

Ethical statement

Animal research was conducted in agreement with the Italian Law (DL 26/2014 of Italian Ministry of Health implementing EU 63/2010) and the recommendations in the *Guide for the Care and Use of Laboratory Animals* of the National Institute of Health. Animal projects were also reviewed and approved by the Animal Care Committee of the University of Trento, Istituto Italiano di Tecnologia and the Italian Ministry of Health (authorization no. 377/20, 07753.28).

Animals

Slc6a8-KO mice (C57BL/6J background; (Baroncelli et al., 2014)) were generated by the European Molecular Biology Laboratory (EMBL). Since CTD is an X-linked disorder, only male mice were used in this study. Mice were housed under controlled humidity (60 ± 10%) and temperature (21 ± 1 °C). Food and water were available *ad libitum*.

Molecular cloning and viral preparation

The full-length human sequence of *SLC6A8* (*hSLC6A8*) was cloned under the control of the small JeT promoter (Tornoe et al., 2002) into a pAAV_WPRE.SV40 using standard molecular biology techniques. An HA tag at the C-terminal of *SLC6A8* was used to facilitate the detection of the transgenic protein. The JeT-hSCL6A8 sequence was synthesized by Twin Helix (Milano, Italy) as reported in Table S2. Serotype 9 adeno-associated viral (AAV) vectors containing pAAV_JeT-hSLC6A8_WPRE.SV40 were produced by the University of Pennsylvania Vector Core (Philadelphia, PA). Viral titration via genome copy number counting was performed using digital droplet PCR. As control, we used an AAV9 containing pAAV_JeT-GFP_WPRE.SV40.

Experimental design

All the experiments were performed on four cohorts of male mice: Slc6a8-KO (n = 21) and WT (n = 10) injected with AAV-hSLC6A8, and Slc6a8-KO (n = 15) and WT (n = 23) injected with AAV-GFP as controls. As depicted in the experimental scheme of Fig. 3, the four cohorts of mice were administered with AAV vectors via intracerebroventricular (i.c.v.) injection at P1. The four experimental groups were subjected to two sessions of fMRI scans, at P40 and P140. Forty-eight hours after each fMRI session mice underwent two behavioral tests. The testing order consisted of self-grooming scoring, followed by the Y maze test. At the end of the experimental schedule, a small group of Slc6a8-KO (n = 5) and WT (n = 2) mice were transcardially perfused with 4% paraformaldehyde and coronal brain sections were acquired with a confocal microscope to assess the expression pattern of the AAV-hSLC6A8 vector. The rest of the experimental mice were sacrificed after the last behavioral test to collect tissues for post-mortem Cr analysis.

AAV injection in newborn mice

Intracerebroventricular injection of AAV was performed as previously described (Kim et al., 2014). Briefly, at P1 pups were placed on ice for few minutes to induce hypothermic anesthesia and then moved onto a cooled stereotaxic frame. Coordinates were adjusted on the base of lambda point of *repere* (X, Y, Z) = (1, ±0.3, -2.0) mm. Pups received bilateral injections of 1 ul of AAV vector ($3x10^9$ vg/mouse) using a glass capillary connected by a tube to a Hamilton syringe placed on a micropump. The AAV solution was infused over a 60s period and the pipette was removed after a delay of 30s to prevent backflow. We allowed the pups to recover from the anesthesia under a heating bulb, before transferring them back to the mother cage.

Neuroimaging assessment

Resting state fMRI data were acquired as extensively described in (Ferrari et al., 2012; Sforazzini et al., 2016; Bertero et al., 2018; Pagani et al., 2019). Briefly, mice were anesthetized with isoflurane (4% induction, 2% maintenance), intubated and artificially ventilated. During resting-state scans, isoflurane was replaced with halothane (0.7%) to obtain light sedation. We used a 7T MRI scanner (Bruker), Bruker Paravision software version 6, a 72-mm birdcage transmit coil and a 4-channel solenoid coil for signal reception (Liska et al., 2015; Montani et al., 2020; Pagani et al., 2021). For each session, in vivo structural images were acquired with a fast spin-echo sequence (repetition time [TR]=5500ms, echo time [TE]=60ms, matrix 192×192, the field of view 2×2cm, 24 coronal slices, slice thickness 500µm). BOLD rsfMRI time series were acquired using an echo planar imaging (EPI) sequence with the following parameters: TR/TE = 1000/15 ms, flip angle 30°, matrix 100 × 100, field of view 2.3 × 2.3cm, 18 coronal slices, slice thickness 600 µm for 1920 volumes (total duration 32 minutes).

Analysis of fMRI timeseries

rsfMRI BOLD time series were preprocessed as previously described (Sforazzini et al., 2014; Pagani et al., 2019, 2021; Montani et al., 2020). We removed the first 50 volumes of each timeseries to allow for signal equilibration. BOLD timeseries were then despiked, motion corrected and spatially registered to a common reference brain template. Mean ventricular signal (corresponding to the averaged BOLD signal within a reference ventricular mask) and motion traces of head realignment parameters (3 translations + 3 rotations) were regressed out from each time series. Finally, we applied a spatial smoothing (full width at half maximum of 0.6 mm) and a band-pass filter to a frequency window of 0.01-0.1 Hz.

Network based statistics (NBS) (Zalesky et al., 2010; Pagani et al., 2019) was carried out by extracting fMRI signal in 85 anatomically parcellated regions (based on the Allen brain Atlas, Table S1). The list of reemployed regions can be found in (Coletta et al., 2020): We next computed an unpaired two-tailed Student's t test for each element of the corresponding correlation matrix separately ($t > 2.7$-3.5). FWER correction at the network level was performed using 5000 random permutations ($p < 0.05$) as implemented in the network-based statistics (NBS) package (Zalesky et

al., 2010; Pagani et al., 2019). The chord plots show the 85 parcels clustered in 9 anatomical meta regions (Table S1). The size of each regional arc is proportional to the number of the parcels in the arc. The link width between two meta regions is proportional, relatively to the meta region size, to the ratio of edges connecting the two regions that significatively changed (blue, reduced number of connections; red, increased number of connections).

rsfMRI connectivity was also probed using seed-based analyses (Montani et al., 2020; Rocchi et al., 2022). A seed region was selected to cover the areas of interest, based on NBS results (Supplementary Figure 5). Voxel-wise intergroup differences in seed-based mapping were assessed using a 2-tailed Student's t test ($|t|>2$, $p<0.05$) and family-wise error (FWE) cluster-corrected using a cluster threshold of $p=0.050$ as implemented in FSL (https://fsl.fmrib.ox.ac.uk/fsl/). The code used for preprocessing and analyzing mouse rsfMRI data is available at: https://github.com/functional-neuroimaging/rsfMRI-preprocessing; https://github.com/functional-neuroimaging/rsfMRI-global-local-connectivity; https://github.com/functional-neuroimaging/rsfMRI-seed-based-mapping

Behavioral tests

Behavioral testing was longitudinally performed in the same mice used for rsfMRI at P40 and P140. The testing order for neurobehavioral assessment consisted of a self-grooming test followed by Y maze. To reduce the potential circadian effects on behavioral performance, testing was carried out during the same time interval each day (1-5 pm). For the analysis of spontaneous self-grooming, mice were individually placed in an open field arena for 20 minutes (40 cm × 40 cm × 40 cm). Sessions were recorded and mice automatically tracked using the ANY-maze software. After a 10-min habituation period, the cumulative time spent by mice grooming themselves was scored for 10 min as an index of stereotypic behavior (McFarlane et al., 2008; Baroncelli et al., 2016). Spatial working memory was tested using the Y-maze, as previously described (Baroncelli et al., 2014, 2016). We used a Y-shaped maze made of solid grey plastic, with three symmetrical arms at a 120-degree angle (35cm long, 5cm wide and 15cm tall). Mice were placed in the center of the arena and allowed to freely explore the maze for 8 minutes. The arena was cleaned with ethanol between trials to avoid the building of odor traces. Sessions were video-recorded and mice were automatically tracked using ANY-maze. In the offline blind analysis, an arm entry was defined when all four limbs of the mouse are within the arm; a triad was defined as a set of three-different-arm entries. Alternation percentage was obtained by dividing the number of triads by the number of possible alternations.

Creatine measurements

Brain samples were homogenized in Phosphate Buffer Saline-Protease inhibitor (100:1) on ice. An aliquot of each brain homogenate was extracted (1:3) with cold CH_3CN containing creatine-(methyl-*d3*) as internal standard and centrifuged at 21.100 x g for 20min at 4°C. A calibration curve

was prepared in Phosphate Buffer Saline containing 20% CH_3CN. The calibrators were extracted as the brain homogenates. The supernatants of the extracted brain homogenates and calibrators were further diluted 100-fold with 2mM NH_4OAc in H2O (pH 8), and analyzed by LC-MS/MS on a Waters ACQUITY UPLC-MS/MS system consisting of a triple quadrupole detector (TQD) mass spectrometer equipped with an electrospray ionization interface (ESI) and a photodiode array λ detector (PDA) from Waters Inc. (Milford, MA, USA). Electrospray ionization was applied in positive mode. Compound-dependent parameters as Multiple Reaction Monitoring (MRM) transitions and collision energy were developed for the parent compound and the internal standard. The analyses were run on an ACE Excel 2 C18 (150x2.1mmID) with an ACE Excel UHPLC Pre-column Filter at 40°C, using 2mM NH4OAc in H2O (pH 8) (A) and CH3CN (B) as mobile phase at 0.2mL/min. A linear gradient was applied starting at 0%B with an initial hold for 3.5min, then 0-80%B in 2min and 80-0%B in 0.1min, followed by a hold for 2.4min at 0%B. All samples were quantified by MRM peak area response factor in order to determine the levels of Cr in the brain samples. The data was normalized by 100mg brain/mL.

Partial Least Square Correlation

We assessed brain-behavior relationship using partial-least square analysis, a multivariate data-driven statistical technique. This analysis aims to maximize the covariance between imaging readouts (in our case, individual seed-based connectivity maps of the anterior cingulate), behavioral scores (i.e. self-grooming and spontaneous alternations) and biochemical data (brain Cr levels) by identifying latent components (LC) that represent the optimal weighted linear combination of the original variables (Krishnan et al., 2011). The null hypothesis that the observed brain-behavior relationship could be due to chance was verified via permutation testing (1,000 iterations) of behavioral and biochemical data matrix. To avoid LCs being trivially driven by inter-group differences, permutations were performed within groups as per previous guidelines (Kebets et al., 2021). The stability of the contribution of each brain and behavioral element was assessed via bootstrapping, where bootstrap resampling was performed within each experimental group to avoid patterns being driven by group differences (Kebets et al., 2019). We tested the existence of a significant correlation between behavioral indexes and fMRI connectivity in the cingulate fMRI network, a network systems that is relevant for all the behaviors assessed (Pagani et al., 2019). Post-mortem brain Cr level assessed at P140 was modeled as a continuous variable in the behavioral matrix to probe whether the multidimensional relationship between connectivity and behavior could be affected by Cr levels.

Acknowledgments

This work was supported by the Telethon foundation (GGP19177 to L. Baroncelli and A. Gozzi). A. Gozzi was also supported by Simons Foundation Grant (SFARI 400101), European Research Council (ERC—DISCONN, No. 802371 and BRAINAMICS, No. 101125054). L. Baroncelli was also supported

by project ECS_00000017 MUR Directoral Decree n.1055, 23 June 2022, CUP B83C22003930001, “Tuscany Health Ecosystem – THE”, Spoke 8 and Italian Ministry of Health, RC 2023.

Supplementary figures and tables

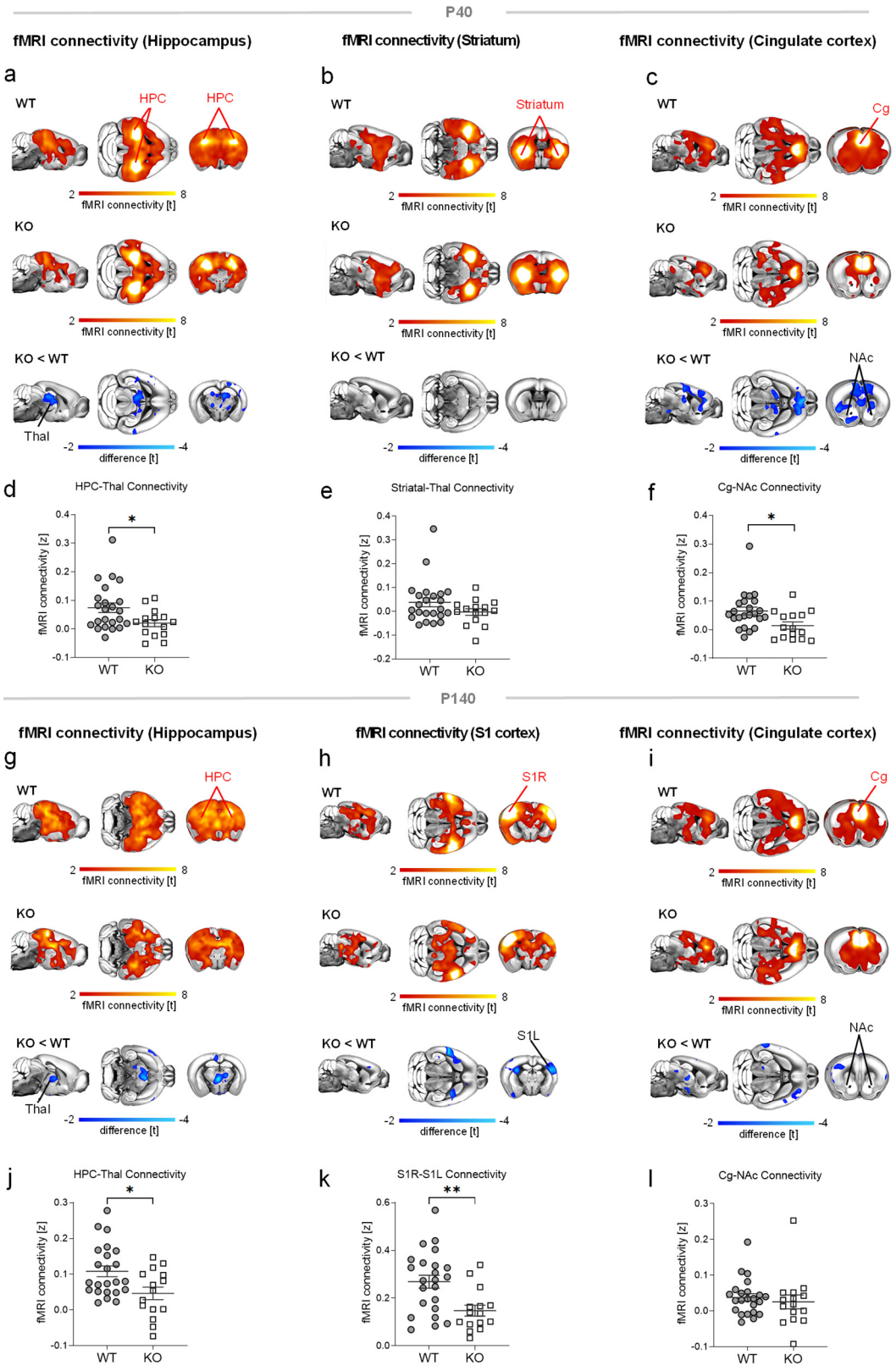

Supplementary Figure 1. Seed-based analysis of fMRI connectivity. *(a-f) Seed-correlation mapping highlighted disrupted hippocampal-thalamus and cingulate cortex connectivity in Slc6a8-KO mice at P40. (g-l) fMRI connectivity in the hippocampal circuit was disrupted also at P140. At this age we also found a prominent reduction of inter-hemispheric somatosensory connectivity. Red/yellow indicates areas in the brain maps exhibiting significant (t> 2.1) fMRI connectivity with seed regions (indicated with red lettering). Blue indicates between-group connectivity differences (t-test, t> 2.1). Corresponding quantifications of connectivity changes in the two groups are reported in panels d-f for P40 (HPC-Thal, t-test, t= 2.35, p= 0.025; Cg-NAc, t-test; t= 2.6, p= 0.014) and j-l for P140 (HPC-Thal, t-test; t= 2.65, p= 0.012; S1R-S1L, t-test; t = 3.17, p = 0.003). HPC, hippocampus; Thal, thalamus; Cg, cingulate cortex; NAc, Nucleus Accumbens; S1R, right somatosensory cortex; S1L, left somatosensory cortex. All statistics are FWE cluster-corrected. FWE, family-wise error. *p < 0.05, **p < 0.01. Error bars indicate SEM and dots represent individual values.*

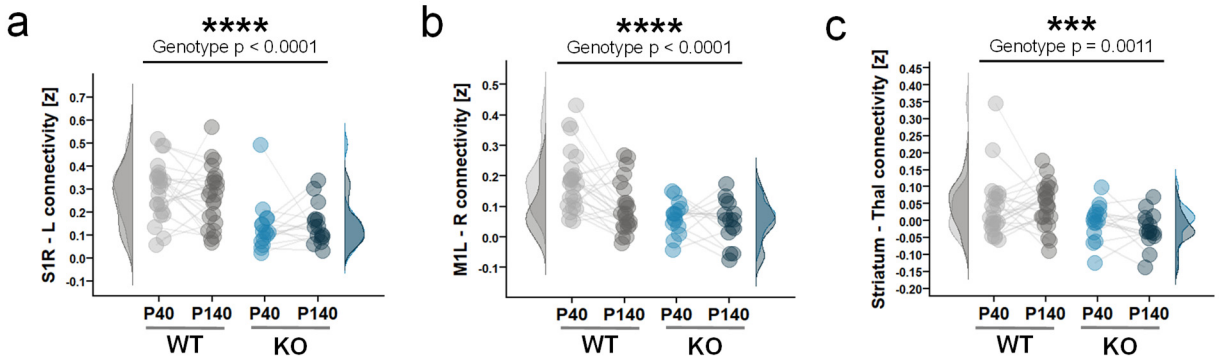

Supplementary Figure 2. Temporal evolution of fMRI connectivity in WT and Slc6a8-KO mice at P40 and P140. *Quantification and distribution of fMRI connectivity in somatosensory (a, Two-way RM ANOVA, genotype factor F = 26, p < 0.0001, genotype x age interaction F = 0.43, p = 0.512) and motor cortices (b, genotype factor F = 14.2, p = 0.0003, genotype x age interaction F = 2.8, p = 0.1) and between striatal and thalamic regions (c, genotype factor, F = 11.4, p = 0.0012, interaction F = 0.85, p = 0.36) in WT and Slc6a8-KO mice administered with AAV-GFP, at P40 and P140. ***p < 0.001, ****p<0.0001. L, left; R, right; M1, motor cortex; S1, somatosensory cortex; Thal, thalamus. Dots represent individual values.*

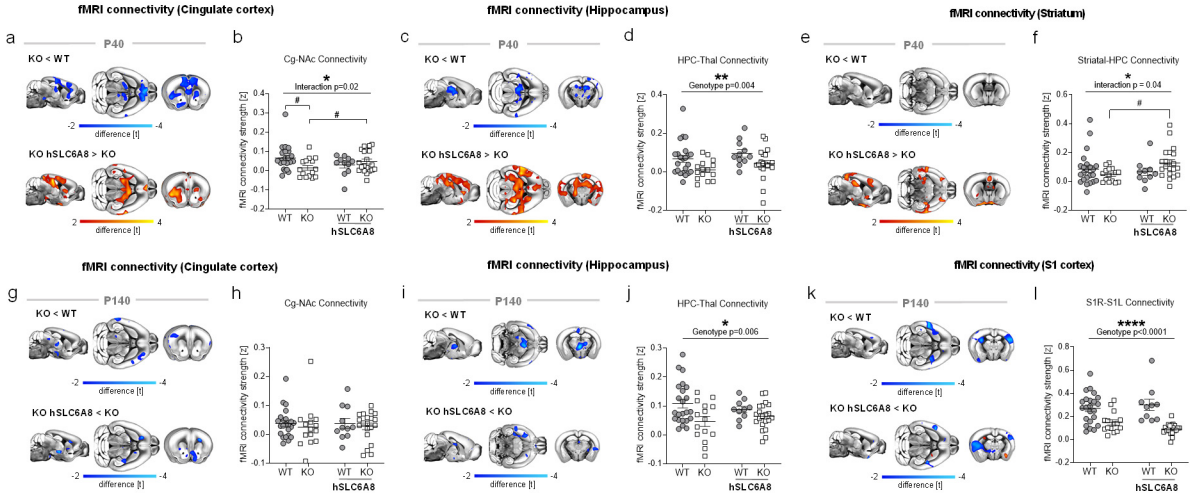

Supplementary Figure 3. AAV-hSLC6A8 treatment rescues fMRI hypo-connectivity in Slc6a8-KO mice. *(a-f) Seed-correlation mapping highlighted rescue of fronto-limbic connectivity at P40 in Slc6a8-KO mice injected with JeT-hSLC6A8. Red/yellow coloring in bottom panels denotes the rescue effects of AAV- hSLC6A8 treatment (t-test, t> 2). Histograms illustrate quantification of connectivity strength between the probed seed and regions of interest (b, Cg-NAc: Two-way ANOVA, genotype x treatment interaction F = 5.76.48, p = 0.019; t-test, # p < 0.05; d, HPC-Thal: Two-way ANOVA, genotype factor F = 9.08, p = 0.004, interaction, F = 0.01, p = 0.91; f, striatal-HPC: Two-way ANOVA, interaction F = 0.26, p = 0.61; t-test, # p < 0.05). (g-l) The same analysis at P140 revealed no rescue of gene therapy (h, Cg-NAc: Two-way ANOVA, interaction F = 0.004, p = 0.95; j, HPC-Thal: Two-way ANOVA, genotype factor F = 8, p = 0.006, interaction, F = 1.64, p = 0.2; l, S1R-S1L: Two-way ANOVA, genotype factor F = 37.3, p < 0.0001, interaction F = 2.64, p = 0.11). HPC, hippocampus; Ins, insula; Thal, thalamus; Cg, cingulate cortex; NAc, Nucleus Accumbens; S1R, right somatosensory cortex 1; S1L, left somatosensory cortex 1. All statistics are FWE cluster-corrected. FWE, family-wise error. For Two-way ANOVA, * p< 0.05, **p< 0.01, ****p < 0.0001. Error bars indicate SEM and dots represent individual values.*

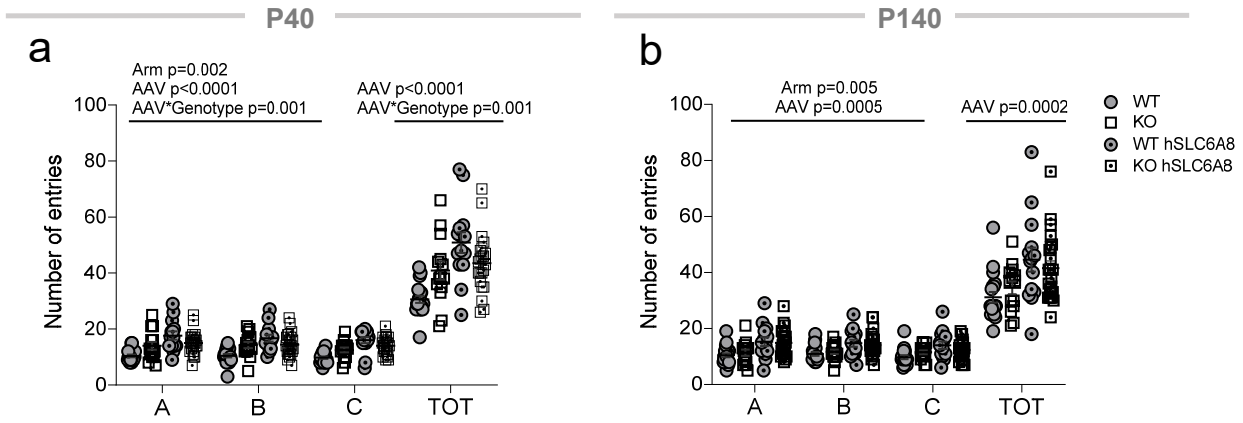

Supplementary Figure 4. Behavioral performance following treatment with AAV-hSLC6A8. *Histograms depict the mean number of entries in the single arms of the maze (A, B, C) and the total number of arm entries (TOT) for the different experimental groups at P40 (a) and P140 (b). An increased number of entries was found in mice injected with AAV-hSLC6A8 both at P40 (single arms: Three-way RM ANOVA, factor AAV $F = 19.8$, $p < 0.0001$; TOT: Two-way ANOVA factor AAV $F= 21$, $p < 0.0001$) and P140 (single arms: Three-way RM ANOVA, factor AAV $F = 13.3$, $p = 0.0005$; TOT: Two-way ANOVA factor AAV $F= 14.9$, $p = 0.0002$).*

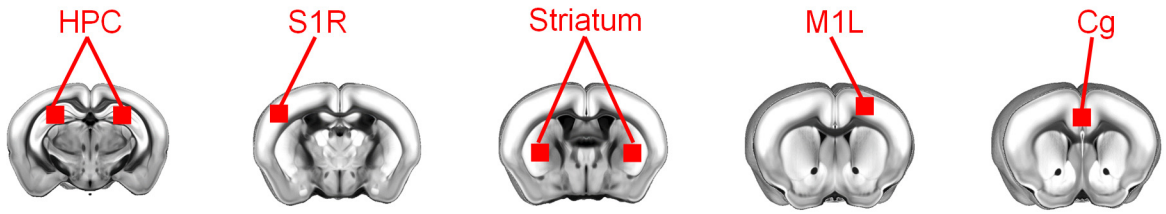

Supplementary Figure 5. Anatomical location of seed regions. *HPC, hippocampus; S1R, right somatosensory cortex 1; M1L, left motor cortex; Cg, cingulate cortex.*

Table S1. Complete list of brain areas (and abbreviations) used for NBS.

85 anatomically parcellated regions (based on the Allen brain Atlas), as in (Coletta et al., 2020). ISO: isocortex, OLF: olfactory region, HPF: hippocampal formation, CTXsp: cortical subplate, STR:striatum, THAL: thalamus, HY: hypothalamus, MID: midbrain

1	MOp	Primary motor area	ISO
2	MOs	Secondary motor area	ISO
3	Ssp	Primary somatosensory area	ISO
4	SSs	Supplemental somatosensory area	ISO
5	GU	Gustatory areas	ISO
6	VISC	Visceral area	ISO
7	AUD	Auditory area	ISO
8	VIS	Visual area	ISO
9	ACAd	Anterior cingulate area, dorsal part	ISO
10	ACAv	Anterior cingulate area, ventral part	ISO
11	PL	Prelimbic area	ISO
12	ILA	Infralimbic area	ISO
13	ORB	Orbital area	ISO
14	AId	Agranular insular area, dorsal part	ISO
15	AIp	Agranular insular area, posterior part	ISO
16	AIv	Agranular insular area, ventral part	ISO
17	RSPagl	Retrosplenial area, lateral agranular part	ISO
18	RSPd	Retrosplenial area, dorsal part	ISO
19	RSPv	Retrosplenial area, ventral part	ISO
20	PTLp	Posterior parietal association areas	ISO
21	TEa	Temporal association areas	ISO
22	PERI	Perirhinal area	ISO
23	ECT	Ectorhinal area	ISO
24	PIR	Piriform area	OLF
25	OLFnuc	olfactory_nuclei	OLF
26	CA	Ammon's horn	HPF
27	DG	Dentate gyrus	HPF
28	ENT	Entorhinal area	HPF
29	RHP	Retro_hippocampal	HPF
30	EndCla	EndopiriformNucleus_Claustrum	CTXsp
31	LA	Lateral amygdalar nucleus	CTXsp
32	BLA	Basolateral amygdalar nucleus	CTXsp
33	BMA	Basomedial amygdalar nucleus	CTXsp
34	PA	Posterior amygdalar nucleus	CTXsp
35	STRd	Striatum dorsal region	STR
36	STRv	Striatum ventral region	STR
37	LSX	Lateral septal complex	STR
38	sAMY	Striatum-like amygdalar nuclei	STR
39	PAL	Pallidum	PAL
40	DORsm	Thalamus, sensory-motor cortex related	THAL
41	DORpm	Thalamus, polymodal association cortex related	THAL
42	PVZ	Periventricular zone	HY

43	PVR	Periventricular region	HY
44	MEZ	Hypothalamic medial zone	HY
45	LZ	Hypothalamic lateral zone	HY
46	MBsen	Midbrain, sensory related	MID
47	MBmot	Midbrain, motor related	MID
48	MBsta	Midbrain, behavioral state related	MID
49	MOp	Primary motor area	ISO
50	MOs	Secondary motor area	ISO
51	Ssp	Primary somatosensory area	ISO
52	SSs	Supplemental somatosensory area	ISO
53	GU	Gustatory areas	ISO
54	VISC	Visceral area	ISO
55	AUD	Auditory area	ISO
56	VIS	Visual area	ISO
57	AId	Agranular insular area, dorsal part	ISO
58	AIp	Agranular insular area, posterior part	ISO
59	AIv	Agranular insular area, ventral part	ISO
60	PTLp	Posterior parietal association areas	ISO
61	TEa	Temporal association areas	ISO
62	PERI	Perirhinal area	ISO
63	ECT	Ectorhinal area	ISO
64	PIR	Piriform area	OLF
65	OLFnuc	olfactory_nuclei	OLF
66	CA	Ammon's horn	HPF
67	DG	Dentate gyrus	HPF
68	ENT	Entorhinal area	HPF
69	RHP	Retro_hippocampal	HPF
70	EndCla	EndopiriformNucleus_Claustrum	CTXsp
71	LA	Lateral amygdalar nucleus	CTXsp
72	BLA	Basolateral amygdalar nucleus	CTXsp
73	BMA	Basomedial amygdalar nucleus	CTXsp
74	PA	Posterior amygdalar nucleus	CTXsp
75	STRd	Striatum dorsal region	STR
76	STRv	Striatum ventral region	STR
77	LSX	Lateral septal complex	STR
78	sAMY	Striatum-like amygdalar nuclei	STR
79	PAL	Pallidum	PAL
80	DORsm	Thalamus, sensory-motor cortex related	THAL
81	DORpm	Thalamus, polymodal association cortex related	THAL
82	LZ	Hypothalamic lateral zone	HY
83	MBsen	Midbrain, sensory related	MID
84	MBmot	Midbrain, motor related	MID
85	MBsta	Midbrain, behavioral state related	MID

Table S2. Full sequence of pAAV-Jet-hSLC6A8

cttccgcttcctcgctcactgactcgctgcgctcggtcgttcggctgcggcgagcggtatcagctcactcaaaggcggtaatacggttatccacagaatc
aggggataacgcaggaaagaacatgtgagcaaaaggccagcaaaaggccaggaaccgtaaaaaggccgcgttgctggcgtttttccataggctccg
ccccccctgacgagcatcacaaaaatcgacgctcaagtcagaggtggcgaaacccgacaggactataaagataccaggcgtttccccctggaagctcc
ctcgtgcgctctcctgttccgaccctgccgcttaccggatacctgtccgcctttctcccttcgggaagcgtggcgctttctcatagctcacgctgtaggtatc
tcagttcggtgtaggtcgttcgctccaagctgggctgtgtgcacgaaccccccgttcagcccgaccgctgcgccttatccggtaactatcgtcttgagtcc
aacccggtaagacacgacttatcgccactggcagcagccactggtaacaggattagcagagcgaggtatgtaggcggtgctacagagttcttgaagtg
gtggcctaactacggctacactagaagaacagtatttggtatctgcgctctgctgaagccagttaccttcggaaaaagagttggtagctcttgatccggc
aaacaaaccaccgctggtagcggtggtttttttgtttgcaagcagcagattacgcgcagaaaaaaaggatctcaagaagatcctttgatcttttctacgg
ggtctgacgctcagtggaacgaaaactcacgttaagggattttggtcatgagattatcaaaaaggatcttcacctagatccttttaaattaaaaatgaag
ttttaaatcaatctaaagtatatatgagtaaacttggtctgacagttaccaatgcttaatcagtgaggcacctatctcagcgatctgtctatttcgttcatcc
atagttgcctgactccccgtcgtgtagataactacgatacgggagggcttaccatctggccccagtgctgcaatgataccgcgagacccacgctcaccg
gctccagatttatcagcaataaaccagccagccggaagggccgagcgcagaagtggtcctgcaactttatccgcctccatccagtctattaattgttgcc
gggaagctagagtaagtagttcgccagttaatagtttgcgcaacgttgttgccattgctacaggcatcgtggtgtcacgctcgtcgtttggtatggcttcat
tcagctccggttcccaacgatcaaggcgagttacatgatcccccatgttgtgcaaaaaagcggttagctccttcggtcctccgatcgttgtcagaagtaa
gttggccgcagtgttatcactcatggttatggcagcactgcataattctcttactgtcatgccatccgtaagatgcttttctgtgactggtgagtactcaacc
aagtcattctgagaatagtgtatgcggcgaccgagttgctcttgcccggcgtcaatacgggataataccgcgccacatagcagaactttaaaagtgctc
atcattggaaaacgttcttcggggcgaaaactctcaaggatcttaccgctgttgagatccagttcgatgtaacccactcgtgcacccaactgatcttcagc
atcttttactttcaccagcgtttctgggtgagcaaaaacaggaaggcaaaatgccgcaaaaaagggaataagggcgacacggaaatgttgaatactca
tactcttcctttttcaatattattgaagcatttatcagggttattgtctcatgagcggatacatatttgaatgtatttagaaaaataaacaaataggggttcc
gcgcacatttccccgaaaagtgccacctaaattgtaagcgttaatattttgttaaaattcgcgttaaatttttgttaaatcagctcatttttttaaccaatagg
ccgaaatcggcaaaatcccttataaatcaaaagaatagaccgagatagggttgagtgttgttccagtttggaacaagagtccactattaaagaacgtgg
actccaacgtcaaagggcgaaaaaccgtctatcagggcgatggcccactacgtgaaccatcaccctaatcaagttttttggggtcgaggtgccgtaaag
cactaaatcggaaccctaaagggagcccccgatttagagcttgacggggaaagccggcgaacgtggcgagaaaggaagggaagaaagcgaaagga
gcgggcgctagggcgctggcaagtgtagcggtcacgctgcgcgtaaccaccacacccgccgcgcttaatgcgccgctacagggcgcgtcccattcgcc
attcaggctgcgcaactgttgggaagggcgatcggtgcgggcctcttcgctattacgccagctgcgcgctcgctcgctcactgaggccgcccgggcaaa
gcccgggcgtcgggcgacctttggtcgcccggcctcagtgagcgagcgagcgcgcagagagggagtggccaactccatcactaggggttccttgtagt
taatgattaacccgccatgctacttatctacgtagccatgctctaggaagagtaccattgacgtcaataatgacgtatgttcccatagtaacgccaatag
ggactttccattgacgtcaatgggtggagtatttacggtaaactgcccacttggcagtacatcaagtgtatcatatggggcggagttagggcggagcca
atcagcgtgcgccgttccgaaagttgccttttatggctgggcggagaatgggcggtgaacgccgatgattatataaggacgcgccgggtgtggcacag
ctagttccgtcgcagccgggatttgggtcgcggttcttgtttgtggggttcggcttctggcgtgtgaccggcggctctagagccaccatggcgaagaaga
gcgccgagaacggcatctatagcgtgtccggcgacgagaagaagggccccctcatcgcgcccgggcccgacggggccccggccaagggcgacggcc
ccgtgggcctggggacacccggcggccgcctggccgtgccgccgcgcgagacctggacgcgccagatggacttcatcatgtcgtgcgtgggcttcgcc
gtgggcttgggcaacgtgtggcgcttcccctacctgtgctacaagaacggcggaggtgtgttccttattccctacgtcctgatcgccctggttggaggaat
ccccattttcttcttagagatctcgctgggccagttcatgaaggccggcagcatcaatgtctggaacatctgtcccctgttcaaaggcctgggctacgcct
ccatggtgatcgtcttctactgcaacacctactacatcatggtgctggcctggggcttctattacctggtcaagtcctttaccaccacgctgccctgggcca
catgtggccacaCctggaacactcccgactgcgtggagatcttccgccatgaagactgtgccaatgccagcctggccaacctcacctgtgaccagcttg
ctgaccgccggtcccctgtcatcgagttctgggagaacaaagtcttgaggctgtctgggggactggaggtgccaggggccctcaactgggaggtgacc
ctttgtctgctggcctgctgggtgctggtctacttctgtgtctggaagggggtcaaatccacgggaaagatcgtgtacttcactgctacattcccctacgtg
gtcctggtcgtgctgctggtgcgtggagtgctgctgcctggcgccctggatggcatcatttactatctcaagcctgactggtcaaagctggggtcccctca
ggtgtggatagatgcggggacccagattttcttttcttacgccattggcctggggccctcacagccctgggcagctacaaccgcttcaacaacaactgc
tacaaggacgccatcatcctggctctcatcaacagtgggaccagcttctttgctggcttcgtggtcttctccatcctgggcttcatggctgcagagcaggg
cgtgcacatctccaaggtggcagagtcagggccgggcctggccttcatcgcctacccgcgggctgtcacgctgatgccagtggccccactctgggctgc

cctgttcttcttcatgctgttgctgcttggtctcgacagccagtttgtaggtgtggagggcttcatcaccggcctcctcgacctcctcccggcctcctactac
ttccgtttccaaagggagatctctgtggccctctgttgtgccctctgctttgtcatcgatctctccatggtgactgatggcgggatgtacgtcttccagctgtt
tgactactactcggccagcggcaccaccctgctctggcaggccttttgggagtgcgtggtggtggcctgggtgtacggagctgaccgcttcatggacga
cattgcctgtatgatcgggtaccgaccttgcccctggatgaaatggtgctggtccttcttcaccccgctggtctgcatgggcatcttcatcttcaacgttgtg
tactacgagccgctggtctacaacaacacctacgtgtacccgtggtggggtgaggccatgggctgggccttcgccctgtcctccatgctgtgcgtgccgc
tgcacctcctgggctgcctcctcagggccaagggcaccatggctgagcgctggcagcacctgacccagcccatctggggcctccaccacttggagtacc
gagctcaggacgcagatgtcaggggcctgaccaccctgaccccagtgtccgagagcagcaaggtcgtcgtggtggagagtgtcatgtacccatacgat
gttccagattacgcatgaggatccgagctcggtaccaagcttatcgataatcaacctctggattacaaaatttgtgaaagattgactggtattcttaacta
tgttgctccttttacgctatgtggatacgctgctttaatgcctttgtatcatgctattgcttcccgtatggctttcattttctcctccttgtataaatcctggttgc
tgtctctttatgaggagttgtggcccgttgtcaggcaacgtggcgtggtgtgcactgtgtttgctgacgcaacccccactggttggggcattgccaccacc
tgtcagctcctttccgggactttcgctttccccctccctattgccacggcggaactcatcgccgcctgccttgcccgctgctggacaggggctcggctgttg
ggcactgacaattccgtggtgttgtcggggaaatcatcgtcctttccttggctgctcgcctgtgttgccacctggattctgcgcgggacgtccttctgctac
gtcccttcggccctcaatccagcggaccttccttcccgcggcctgctgccggctctgcggcctcttccgcgtcttcgccttcgccctcagacgagtcggatc
tccctttgggccgcctccccgcatcgataccgtcgacccgggcggccgcttcgagcagacatgataagatacattgatgagtttggacaaaccacaact
agaatgcagtgaaaaaaatgctttatttgtgaaatttgtgatgctattgctttatttgtaaccattataagctgcaataaacaagttaacaacaacaattg
cattcattttatgtttcaggttcagggggagatgtgggaggttttttaaagcaagtaaaacctctacaaatgtggtaaaatcgataaggatcttcctagag
catggctacgtagataagtagcatggcgggttaatcattaactacaaggaacccctagtgatggagttggccactccctctctgcgcgctcgctcgctca
ctgaggccgggcgaccaaaggtcgcccgacgcccgggctttgcccgggcggcctcagtgagcgagcgagcgcgcagctgcattaatgaatcggccaa
cgcgcggggagaggcggtttgcgtattgggcgct

References

Baker SA, Gajera CR, Wawro AM, Corces MR, Montine TJ (2021) GATM and GAMT synthesize creatine locally throughout the mammalian body and within oligodendrocytes of the brain. Brain Res 1770.

Baroncelli L, Alessandrì MG, Tola J, Putignano E, Migliore M, Amendola E, Gross C, Leuzzi V, Cioni G, Pizzorusso T (2014) A novel mouse model of creatine transporter deficiency. F1000Research 3 Available at: https://pubmed.ncbi.nlm.nih.gov/25485098/ [Accessed January 4, 2023].

Baroncelli L, Braschi C, Spolidoro M, Begenisic T, Maffei L, Sale A (2011) Brain plasticity and disease: A matter of inhibition. Neural Plast 2011.

Baroncelli L, Molinaro A, Cacciante F, Alessandrı MG, Napoli D, Putignano E, Tola J, Leuzzi V, Cioni G, Pizzorusso T (2016) A mouse model for creatine transporter deficiency reveals early onset cognitive impairment and neuropathology associated with brain aging. Hum Mol Genet 25:4186–4200 Available at: https://pubmed.ncbi.nlm.nih.gov/27466184/ [Accessed January 4, 2023].

Battini R, Alessandrì MG, Casalini C, Casarano M, Tosetti M, Cioni G (2017) Fifteen-year follow-up of Italian families affected by arginine glycine amidinotransferase deficiency. Orphanet J Rare Dis 12.

Bertero A, Liska A, Pagani M, Parolisi R, Masferrer ME, Gritti M, Pedrazzoli M, Galbusera A, Sarica A, Cerasa A, Buffelli M, Tonini R, Buffo A, Gross C, Pasqualetti M, Gozzi A (2018) Autism-associated 16p11.2 microdeletion impairs prefrontal functional connectivity in mouse and human. Brain 141:2055–2065 Available at: https://pubmed.ncbi.nlm.nih.gov/29722793/.

Braissant O, Béard E, Torrent C, Henry H (2010) Dissociation of AGAT, GAMT and SLC6A8 in CNS: Relevance to creatine deficiency syndromes. Neurobiol Dis 37.

Cacciante F, Gennaro M, Sagona G, Mazziotti R, Lupori L, Cerri E, Putignano E, Butt M, Do MHT, McKew JC, Alessandrì MG, Battini R, Cioni G, Pizzorusso T, Baroncelli L (2020) Cyclocreatine treatment ameliorates the cognitive, autistic and epileptic phenotype in a mouse model of Creatine Transporter Deficiency. Sci Rep 10.

Chen X, Dong T, Hu Y, Shaffo FC, Belur NR, Mazzulli JR, Gray SJ (2022) AAV9/MFSD8 gene therapy is effective in preclinical models of neuronal ceroid lipofuscinosis type 7 disease. J Clin Invest 132.

Chen X, Lim DA, Lawlor MW, Dimmock D, Vite CH, Lester T, Tavakkoli F, Sadhu C, Prasad S, Gray SJ (2023) Biodistribution of Adeno-Associated Virus Gene Therapy Following Cerebrospinal Fluid-Directed Administration. Hum Gene Ther 34.

Coletta L, Pagani M, Whitesell JD, Harris JA, Bernhardt B, Gozzi A (2020) Network structure of the mouse brain connectome with voxel resolution. Sci Adv 6 Available at: https://pubmed.ncbi.nlm.nih.gov/33355124/ [Accessed October 6, 2021].

Ferrari L, Turrini G, Crestan V, Bertani S, Cristofori P, Bifone A, Gozzi A (2012) A robust experimental protocol for pharmacological fMRI in rats and mice. J Neurosci Methods 204:9–18 Available at: http://www.ncbi.nlm.nih.gov/pubmed/22068031 [Accessed March 24, 2020].

Fries P (2015) Rhythms for Cognition: Communication through Coherence. Neuron 88.

Ghirardini E, Calugi F, Sagona G, Di Vetta F, Palma M, Battini R, Cioni G, Pizzorusso T, Baroncelli L (2021) The role of preclinical models in creatine transporter deficiency: Neurobiological mechanisms, biomarkers and therapeutic development. Genes (Basel) 12.

Ghirardini E, Sagona G, Marquez-Galera A, Calugi F, Navarron CM, Cacciante F, Chen S, Di Vetta F, Dadà L, Mazziotti R, Lupori L, Putignano E, Baldi P, Lopez-Atalaya JP, Pizzorusso T, Baroncelli L (2023) Cell-specific vulnerability to metabolic failure: the crucial role of parvalbumin expressing neurons in creatine transporter deficiency. Acta Neuropathol Commun 11.

Gozzi A, Schwarz AJ (2016) Large-scale functional connectivity networks in the rodent brain. Neuroimage 127:496–509 Available at: http://www.ncbi.nlm.nih.gov/pubmed/26706448.

Gozzi A, Zerbi V (2022) Modelling brain dysconnectivity in rodents. Biol Psychiatry:ISSN 0006-3223.

Hautman ER, Kokenge AN, Udobi KC, Williams MT, Vorhees C V., Skelton MR (2014) Female mice heterozygous for creatine transporter deficiency show moderate cognitive deficits. J Inherit Metab Dis 37.

Joncquel-Chevalier Curt M, Voicu PM, Fontaine M, Dessein AF, Porchet N, Mention-Mulliez K, Dobbelaere D, Soto-Ares G, Cheillan D, Vamecq J (2015) Creatine biosynthesis and transport in health and disease. Biochimie 119.

Kalueff A V., Stewart AM, Song C, Berridge KC, Graybiel AM, Fentress JC (2015) Neurobiology of rodent self-grooming and its value for translational neuroscience. Nat Rev Neurosci 2015 171 17:45–59 Available at: https://www.nature.com/articles/nrn.2015.8 [Accessed July 13, 2021].

Kebets V, Favre P, Houenou J, Polosan M, Perroud N, Aubry JM, Van De Ville D, Piguet C (2021) Fronto-limbic neural variability as a transdiagnostic correlate of emotion dysregulation. Transl Psychiatry 11.

Kebets V, Holmes AJ, Orban C, Tang S, Li J, Sun N, Kong R, Poldrack RA, Yeo BTT (2019) Somatosensory-Motor Dysconnectivity Spans Multiple Transdiagnostic Dimensions of Psychopathology. Biol Psychiatry 86.

Khoja S, Lambert J, Nitzahn M, Eliav A, Zhang YC, Tamboline M, Le CT, Nasser E, Li Y, Patel P, Zhuravka I, Lueptow LM, Tkachyova I, Xu S, Nissim I, Schulze A, Lipshutz GS (2022) Gene therapy for guanidinoacetate methyltransferase deficiency restores cerebral and myocardial creatine while resolving behavioral abnormalities. Mol Ther Methods Clin Dev 25:278 Available at: /pmc/articles/PMC9051621/ [Accessed August 1, 2023].

Kim JY, Grunke SD, Levites Y, Golde TE, Jankowsky JL (2014) Intracerebroventricular viral injection of the neonatal mouse brain for persistent and widespread neuronal transduction. J Vis Exp Available at: https://pubmed.ncbi.nlm.nih.gov/25286085/ [Accessed May 14, 2023].

Krishnan A, Williams LJ, McIntosh AR, Abdi H (2011) Partial Least Squares (PLS) methods for neuroimaging: A tutorial and review. Neuroimage 56.

Liska A, Bertero A, Gomolka R, Sabbioni M, Galbusera A, Barsotti N, Panzeri S, Scattoni ML, Pasqualetti M, Gozzi A (2018) Homozygous loss of autism-risk gene CNTNAP2 results in reduced local and long-range prefrontal functional connectivity. Cereb Cortex 28:1141–1153.

Liska A, Galbusera A, Schwarz AJ, Gozzi A (2015) Functional connectivity hubs of the mouse brain. Neuroimage 115:281–291.

Marek S et al. (2022) Reproducible brain-wide association studies require thousands of individuals. Nature 603.

Mazziotti R, Cacciante F, Sagona G, Lupori L, Gennaro M, Putignano E, Alessandrì MG, Ferrari A, Battini R, Cioni G, Pizzorusso T, Baroncelli L (2020) Novel translational phenotypes and biomarkers for creatine transporter deficiency. Brain Commun 2 Available at: https://pubmed.ncbi.nlm.nih.gov/32954336/ [Accessed June 11, 2023].

McFarlane HG, Kusek GK, Yang M, Phoenix JL, Bolivar VJ, Crawley JN (2008) Autism-like behavioral phenotypes in BTBR T+tf/J mice. Genes, Brain Behav 7.

McIntosh AR, Bookstein FL, Haxby J V., Grady CL (1996) Spatial pattern analysis of functional brain images using partial least squares. Neuroimage 3.

Montani C, Canella C, Schwarz AJ, Li J, Gilmour G, Galbusera A, Wafford K, Gutierrez-Barragan D, McCarthy A, Shaw D, Knitowski K, McKinzie D, Gozzi A, Felder C (2020) The M1/M4 preferring muscarinic agonist xanomeline modulates functional connectivity and NMDAR antagonist-induced changes in the mouse brain. Neuropsychopharmacology Available at: https://pubmed.ncbi.nlm.nih.gov/33342996/.

Owen JP, Li YO, Yang FG, Shetty C, Bukshpun P, Vora S, Wakahiro M, Hinkley LBN, Nagarajan SS, Sherr EH, Mukherjee P (2013) Resting-state networks and the functional connectome of the human brain in agenesis of the corpus callosum. Brain Connect 3.

Pagani M, Barsotti N, Bertero A, Trakoshis S, Ulysse L, Locarno A, Miseviciute I, De Felice A, Canella C, Supekar K, Galbusera A, Menon V, Tonini R, Deco G, Lombardo M V., Pasqualetti M, Gozzi A (2021) mTOR-related synaptic pathology causes autism spectrum disorder-associated functional hyperconnectivity. Nat Commun 2021 121 12:1–15 Available at: https://www.nature.com/articles/s41467-021-26131-z.

Pagani M, Bertero A, Liska A, Galbusera A, Sabbioni M, Barsotti N, Colenbier N, Marinazzo D, Scattoni ML, Pasqualetti M, Gozzi A (2019) Deletion of autism risk gene shank3 disrupts prefrontal connectivity. J Neurosci 39:5299–5310 Available at: https://doi.org/10.1523/JNEUROSCI.2529-18.2019.

Rocchi F, Canella C, Noei S, Gutierrez-Barragan D, Coletta L, Galbusera A, Stuefer A, Vassanelli S, Pasqualetti M, Iurilli G, Panzeri S, Gozzi A (2022) Increased fMRI connectivity upon chemogenetic inhibition of the mouse prefrontal cortex. Nat Commun 2022 131 13:1–15 Available at: https://www.nature.com/articles/s41467-022-28591-3.

Roland JL, Snyder AZ, Hacker CD, Mitra A, Shimony JS, Limbrick DD, Raichle ME, Smyth MD, Leuthardt EC (2017) On the role of the corpus callosum in interhemispheric functional connectivity in humans. Proc Natl Acad Sci U S A 114.

Salomons GS, Van Dooren SJM, Verhoeven NM, Cecil KM, Ball WS, Degrauw TJ, Jakobs C (2001) X-linked creatine-transporter gene (SLC6A8) defect: A new creatine-deficiency syndrome. Am J Hum Genet 68.

Saunders A, Macosko EZ, Wysoker A, Goldman M, Krienen FM, de Rivera H, Bien E, Baum M, Bortolin L, Wang S, Goeva A, Nemesh J, Kamitaki N, Brumbaugh S, Kulp D, McCarroll SA (2018) Molecular Diversity and Specializations among the Cells of the Adult Mouse Brain. Cell 174.

Schulze A, Battini R (2007) Pre-symptomatic treatment of creatine biosynthesis defects. Subcell Biochem 46.

Sforazzini F, Bertero A, Dodero L, David G, Galbusera A, Scattoni ML, Pasqualetti M, Gozzi A (2016) Altered functional connectivity networks in acallosal and socially impaired BTBR mice. Brain Struct Funct 221:941–954 Available at: https://pubmed.ncbi.nlm.nih.gov/25445840/ [Accessed March 9, 2021].

Sforazzini F, Schwarz AJ, Galbusera A, Bifone A, Gozzi A (2014) Distributed BOLD and CBV-weighted resting-state networks in the mouse brain. Neuroimage 87:403–415.

Siffredi V, Preti MG, Kebets V, Obertino S, Leventer RJ, Mcilroy A, Wood AG, Anderson V, Spencer-Smith MM, Van De Ville D (2021) Structural Neuroplastic Responses Preserve Functional

Connectivity and Neurobehavioural Outcomes in Children Born without Corpus Callosum. Cereb Cortex 31.

Sohal VS, Zhang F, Yizhar O, Deisseroth K (2009) Parvalbumin neurons and gamma rhythms enhance cortical circuit performance. Nature 459.

Stöckler S, Hanefeld F, Frahm J (1996) Creatine replacement therapy in guanidinoacetate methyltransferase deficiency, a novel inborn error of metabolism. Lancet 348.

Tornoe J, Kusk P, Johansen TE, Jensen PR (2002) Generation of a synthetic mammalian promoter library by modification of sequences spacing transcription factor binding sites. Gene 297.

Udobi KC, Delcimmuto N, Kokenge AN, Abdulla ZI, Perna MK, Skelton MR (2019) Deletion of the creatine transporter gene in neonatal, but not adult, mice leads to cognitive deficits. J Inherit Metab Dis 42.

van de Kamp JM et al. (2013) Phenotype and genotype in 101 males with x-linked creatine transporter deficiency. J Med Genet 50.

van de Kamp JM, Mancini GM, Salomons GS (2014) X-linked creatine transporter deficiency: clinical aspects and pathophysiology. J Inherit Metab Dis 37.

Van De Kamp JM, Mancini GMS, Pouwels PJW, Betsalel OT, Van Dooren SJM, De Koning I, Steenweg ME, Jakobs C, Van Der Knaap MS, Salomons GS (2011) Clinical features and X-inactivation in females heterozygous for creatine transporter defect. Clin Genet 79.

Womelsdorf T, Schoffelen JM, Oostenveld R, Singer W, Desimone R, Engel AK, Fries P (2007) Modulation of neuronal interactions through neuronal synchronization. Science (80-) 316.

Yao Z et al. (2021) A transcriptomic and epigenomic cell atlas of the mouse primary motor cortex. Nature 598.

Zalesky A, Fornito A, Bullmore ET (2010) Network-based statistic: Identifying differences in brain networks. Neuroimage 53:1197–1207 Available at: https://pubmed.ncbi.nlm.nih.gov/20600983/ [Accessed October 6, 2021].

Zerbi V, Pagani M, Markicevic M, Matteoli M, Pozzi D, Fagiolini M, Bozzi Y, Galbusera A, Scattoni ML, Provenzano G, Banerjee A, Helmchen F, Basson MA, Ellegood J, Lerch JP, Rudin M, Gozzi A, Wenderoth N (2021) Brain mapping across 16 autism mouse models reveals a spectrum of functional connectivity subtypes. Mol Psychiatry Available at: https://doi.org/10.1038/s41380-021-01245-4.